Structural phase transition below 250 K in superconducting K$_{0.75}$Fe$_{1.75}$Se$_2$

A. Ignatov,[1] A. Kumar,[1] P. Lubik,[1] R. H. Yuan,[2] W. T. Guo,[2] N. L. Wang,[2] K. Rabe,[1] and G. Blumberg[1]

[1]*Department of Physics and Astronomy, Rutgers, The State University of New Jersey, Piscataway, New Jersey 08854, USA*
[2]*Beijing National Laboratory for Condensed Matter Physics, Institute of Physics, Chinese Academy of Sciences, Beijing 100190, China*

Vibrational properties of iron-chalcogenide superconductor K$_{0.75}$Fe$_{1.75}$Se$_2$ with $T_c \sim 30$ K have been measured by Raman and optical spectroscopies over the temperature range 3–300 K. The sample undergoes $I4/m \rightarrow I4$ structural phase transition accompanied by loss of inversion symmetry at T_1, below 250 K, observed as the appearance of new fully symmetric Raman mode at $\sim$165 cm^{-1}. Small vibration mode anomalies are also observed at $T_2 \sim 160$ K. From first-principles vibrational analysis of antiferromagnetic K$_{0.8}$Fe$_{1.6}$Se$_2$ utilizing pseudopotentials all observed Raman and infrared modes have been assigned and the displacement patterns of the new Raman mode identified as involving predominantly the Se atoms.

PACS number(s): 78.30.−j, 74.70.Xa, 74.25.Kc

I. INTRODUCTION

Discovery of high-T_c superconductivity in iron-based chalcogenides A_yFe$_{1.6+x}$Se$_2$ (A = K, Rb, Cs, and Tl) (Ref. 1) raised considerable attention since the materials exhibit unusual physical properties. The parent compound (y =1, x =0) is an insulator,[2,3] crystalizes into $\sqrt{5} \times \sqrt{5} \times 1$ $I4/m$ Fe vacancy-ordering structure, and exhibits antiferromagnetic (AFM) order below a Néel temperature of $\sim$560 K.[4] Doping with alkaline metals or Tl ($y < 1$) apparently preserves the Fe vacancy ordering and gives rise to superconductivity in samples with close to 2:4:5 stoichiometry.[5] Early transport[2] and neutron-diffraction[4] studies suggested that the superconductivity coexists with AFM order. Alternatively, the doping is discussed in terms of microscopic phase separation:[6–10] a mixture of vacancy-ordered AFM insulating phase and superconducting phase (SC). Due to resent experimental evidences[11–14] the consensus seems to emerge: the AFM and SC phases are specially separated, the AFM phase occupies from $\sim$80 (Ref. 11) to 95 % (Ref. 12) of the sample volume, and the SC phase is homogeneous and does not contain Fe vacancies or magnetic moments.[12–14]

Raman-scattering study of superconducting K$_{0.8}$Fe$_{1.6}$Se$_2$ observed at least 13 phonon modes.[15] The crystal symmetry of sample was determined as C_{4h} or lower. Zhang *et al.* performed LDA vibration analysis of nonmagnetic $I4/m$ K$_{0.8}$Fe$_{1.6}$Se$_2$ phase and assigned majority of observed Raman modes. The vibrational properties K$_{0.88}$Fe$_{1.63}$S$_2$ isostructural to K$_{0.8}$Fe$_{1.6}$Se$_2$ confirmed Fe-vacancy ordering: 14 Raman-active modes predicted by factor-group analysis were observed and assigned. The authors concluded that the phonon energies in the range 80–300 K are driven by anharmonicity effects without any signatures of electron-phonon interaction.[16] The impact of iron and potassium composition on Raman vibration spectra of $A_{0.8}$Fe$_{1.6}$Se$_2$ (A = K, Rb, and Tl) was presented in Ref. 17.

The optical studies to date showed at least ten IR-active modes at low temperatures.[18,19] The in-plane optical conductivity of (T_c = 31 K) is incoherent at 300 K, dominated by IR-active modes and high-frequency excitations,[19] but become coherent just above the T_c. Small carrier concentration prompted authors[10,19] to suggest that the global superconductivity is due to Josephson coupling of the nanoscale-

sized superconducting phase in the AFM ordered insulating phase.

In this paper we report on Raman-scattering and *ab*-plain optical conductivity studies of superconducting K$_{0.75}$Fe$_{1.75}$Se$_2$ ($T_c \sim$30 K) in the T range 3–300 K. At least 19 Raman-active and 12 IR-active modes are observed at 3 K. The $\sim$136-, 143-, 242-, and 277-cm^{-1} Raman and $\sim$208-cm^{-1} IR mode exhibit Fano-like shape. The Raman Fano modes are due to the vibration coupling to AFM spin fluctuations, while the IR mode is coupled to charge carriers in the low-frequency part of optical conductivity. The Raman phonon linewidth contains approximately equal contributions of two-phonon lattice anharmonicity on one hand and bare self-energy and broadening due to intrinsic defects on the other hand, except for the $\sim$100-cm^{-1} mode dominated by inhomogeneous broadening. We show that K$_{0.75}$Fe$_{1.75}$Se$_2$ undergoes $I4/m \rightarrow I4$ structural phase transition at T_1 below 250 K. Several modes which are not Raman and IR active in the measured geometry in $I4/m$ become clearly visible in the $I4$ phase. Symmetry of the Se-Fe slab is broken at T_1. At $T_2 \sim 160$ K Raman vibration modes exhibit weak anomalies seen as a small discontinuity of vibration frequencies and change in vibration intensity vs temperature dependencies. Raman vibration intensities of a few modes increases between T_1 and T_2, saturating above the T_2, except for three modes dominated by c-axis atomic displacements: c-axis structural distortions within the slab appear to build up on cooling down to 3 K. The low-frequency optical conductivity displays weak temperature dependence above T_1 followed by faster increase below the T_2.

II. EXPERIMENT

The crystal of iron-chalcogenide superconductors were grown by a self-melting method with nominal concentration of 0.8:2.1:2.0 (K:Fe:Se). The actual chemical composition was determined by energy dispersive x-ray spectroscopy as K$_{0.75}$Fe$_{1.75}$Se$_2$ (KFS). Two-step transitions were seen in the resistivity curve,[10] a sharp drop at 42 K is followed by a major superconducting transition with $T_c \sim$30 K. Further details of sample characterization can be found elsewhere.[10]

KFS crystals were never exposed to air. A sealed vial was open under 99.999% N$_2$, the crystal removed and glued

on a replaceable copper sample holder of a helium Oxford Instruments cryostat, dried and cleaved along the *ab* plane, transferred to the He-flow cryostat, and quickly cooled below water-freezing temperature. Raman data were obtained on two single crystals. Data presented in this paper refer to the sample with more detailed temperature dependence records. It is worth mentioning that results obtained on the second sample are consistent with findings reported here.

Raman spectra were excited with a Kr^+ laser line of $\lambda = 647.1$ nm ($E = 1.92$ eV) with less than 10 mW of incident laser power focused into a spot of $\sim 50 \times 100$ μm^2 on the freshly cleaved *ab*-plain crystal surface. The scattered light collected close to the backscattered geometry was focused to 100×240 μm^2 entrance slits of a custom triple-stage spectrometer equipped with 1800 lines/mm gratings. The instrumental resolution was ~ 1.4 cm^{-1}. To record symmetry resolved Raman spectra we employed circularly polarized light with the optical configurations selecting either the same or opposite chirality for incident and scattered light. The former is referred to as right-right (RR) and the latter as right-left (RL) configurations. For the C_{4h} point group the B_g (A_g) symmetry is probed in the RL (RR) scattering geometry. Temperature-dependent Raman spectra were collected at 3, 45, 100, 150, 160, 180, 200, 260, and 300 K with T stability better than 0.1 K. An estimated local heating in the laser spot did not exceed 4 K.

Optical measurements were done by Bruker Vertex 80v spectrometer in the frequency range 25–10 000 cm^{-1}. The sample was under vacuum of 2×10^{-5} Pa. An *in situ* gold and aluminum overcoating technique was used to get the reflectance $R(\omega)$ for light polarized in the KFS (*ab*) planes. The real part of conductivity $\sigma_1(\omega)$ was obtained by the Kramers-Kronig transformation of the $R(\omega)$. Optical spectra were collected at 8, 35, 170, and 300 K.

III. RESULTS

$K_{0.8}Fe_{1.6}Se_2$ crystalizes into tetragonal structure $I4/m$ (space group 87) Ref. [4], resulting in the irreducible vibrational representation:

$$\Gamma_{\text{vib}} = 9A_g \oplus 8B_g \oplus 8E_g \oplus 9A_u \oplus 7B_u \oplus 10E_u. \quad (1)$$

All *g* modes are Raman active, but only the A_g and B_g are selected with RR and RL polarizations under the measured geometry. The A_u and E_u vibrations are infrared active along the *c* axis and in the *ab* plane. The B_u modes are silent. The Fe(1)-vacancy related vibration modes are excluded. Throughout this paper we adopted commonly used site designation: K(1), K(2), Fe(1), Fe(2), Se(1), and Se(2) stand, respectively, for Wyckoff positions of $2a$, $8h$, $4d$, $16i$, $4e$, and $16i$; refer to the legend of Fig. 1.

Raman spectra of $K_{0.75}Fe_{1.75}Se_2$ are shown in Figs. 1(a) and 1(b) for RL and RR polarizations, respectively. At 300 K, at least 7 (9) modes are observed in RL (RR) in good agreement with $9A_g + 8B_g$ expected in the $I4/m$ $\sqrt{5} \times \sqrt{5}$ cell of $K_{0.8}Fe_{1.6}Se_2$.[15] The A_g modes at ~ 112 and 267 cm^{-1} are dominated by both chiral and breathing displacements of K(2) and Fe(2) atoms, respectively; Figs. 1(d) and 1(e). Below 200 K new modes appear (marked with red arrows): at ~ 201 cm^{-1} in RL and at ~ 165 and ~ 211 cm^{-1} in the RR.

The ~ 136- and ~ 277-cm^{-1} phonons in the RL and ~ 144- and ~ 242-cm^{-1} phonons in RR exhibit Fano shapes in the whole temperature range of this study. The Fano modes become more symmetric with temperature decrease. Phonon mode parameters are derived from least-square fit to experimental data and are summarized in Table I.

Low-frequency region of optical conductivity adopted from Fig. 2 in Ref. [10] is shown in Fig. 1(c). In agreement with previous studies,[10,19] $\sigma_1(\omega)$ is small (characteristic of a poor metal) and it is dominated by the infrared-active vibrations and interband features at higher energies. At 170 and 300 K, nine IR-active modes are observed. The ~ 208-cm^{-1} mode exhibits a Fano-like shape, becoming more asymmetric on cooling. At 170 K and below, at least three new modes (red arrows) are formed; Fig. 1(c). An inspection of Table I reveled that Raman and IR modes reported in this work do not overlap. It is therefore tempting to conclude that inversion symmetry is preserved. In Sec. IV we argue that inversion symmetry is actually broken below $T_1 \sim 250$ K. The conductivity displays relatively weak temperature dependence above 170 K followed by about a twofold increase of the continuum as temperature drops from 170 to 35 K. In agreement with previous studies,[18,19] a Drude-like peak is seen in 35-K data, shortly before the sample becomes superconducting.

A. First-principles phonon modes analysis

We performed first-principles density functional theory (DFT) calculations using local-density approximation (LDA) with Perdew Zunger (PZ) parametrization for the exchange-correlation energy functional as implemented in the QUANTUM ESPRESSO simulation package.[20] We used ultrasoft pseudopotentials[21] for K, Fe and norm-conserving pseudopotential[22] for Se to describe the interaction between the ionic cores and the valence electrons. The pseudopotentials include 9 valence electrons for K ($3s^2$, $3p^6$, $4s^2$), 16 for Fe ($3s^2$, $3p^6$, $3d^6$, $4s^2$), and 6 for Se ($4s^2$, $4p^4$) atoms. We used a plane-wave basis with energy cutoff of 40 Ry for wave function and 360 Ry for the change density and a $6 \times 6 \times 4$ Monkhorst Pack[23] k-point mesh for the Brillouin zone (BZ) integration.

We optimized the structure of $K_{0.8}Fe_{1.6}Se_2$ with a four spin cluster AFM ordering as discussed by Bao *et al.*[4] using experimental lattice constants obtained at 11 K. The calculation was done using a primitive unit cell of 22 atoms with K(1) and Fe(1) vacancies at $2a$ and $4b$ Wyckoff sites of space group $I4/m$, respectively. Structural optimization is carried through minimization of energy using Hellman-Feynman forces at each atoms in Broyden-Flecher-Goldfarb-Shanno scheme. The optimized structure shows a very good agreement with the experiment. We also allowed inversion symmetry-breaking displacement and found that $I4$ structure has slightly lower energy (3.5 meV) compared to $I4/m$, however the splitting of atomic coordinates was very small. We find that both the structures exhibit a band gap of ~ 0.4 eV.

Frequencies of the zone center phonons are determined using the linear-response method[24] for the relaxed structures are listed in the first column of Table I for the AFM $I4/m$ $K_{0.8}Fe_{1.6}Se_2$. Since all nine A_g modes anticipated in the parent AFM $I4/m$ $K_{0.8}Fe_{1.6}Se_2$ are observed at room temperature, there is a unique correspondence between computed and
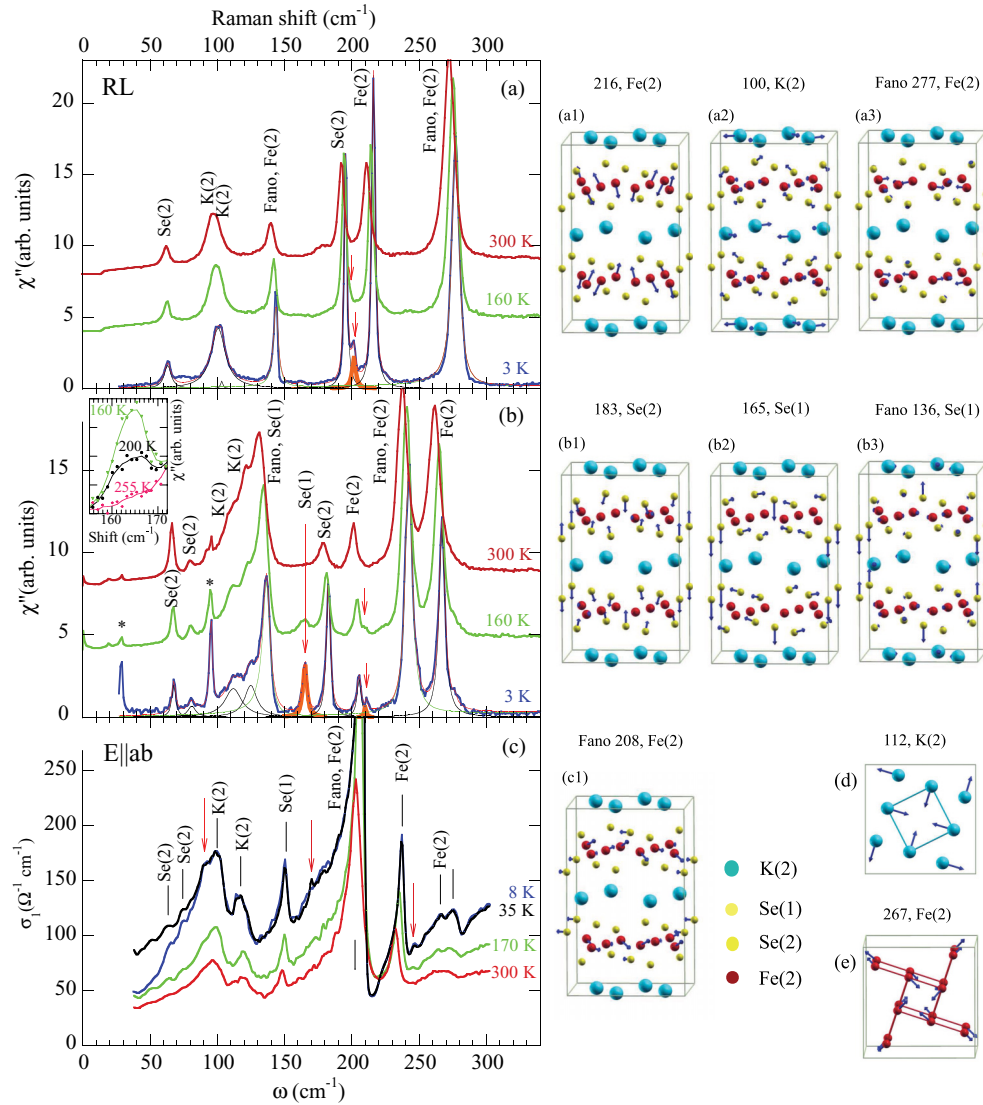
FIG. 1. (Color online) Raman response function of $K_{0.75}Fe_{1.75}Se_2$ in (a) RL and (b) RR channels at 3 (blue), 160 (green), and 300 K (red). (c) *ab*-plane optical conductivity of $K_{0.75}Fe_{1.75}Se_2$ from the same batch of samples at 8, 35, 170, and 300 K, adopted from Fig. 2 in Ref. 10. Fits are illustrated on the 3-K spectra. Modes belonging to $I4/m$ Ref. 4 are shown in black (Lorentz) and green (Fano). New phonons appearing at T_1 in the range 200–255 K [inset in (b)], usually referred to as seen below $\sim$250 K, are shown in orange and marked with arrows. Predominant atomic contribution is labeled for each vibration mode. Computed displacement patterns of selected Raman modes in AFM $I4/m$, $\sqrt{5} \times \sqrt{5}$ unit cells of $K_{0.8}Fe_{1.6}Se_2$ are shown to the right from the vibration spectra: The B_g modes at $\sim$216 and 100 cm^{-1} and Fano mode at 277 cm^{-1} are visualized in (a1)–(a3). The displacement patterns of A_g mode at $\sim$183, A_u mode at $\sim$165 (becomes Raman-active A mode below T_1), and Fano A_g mode at $\sim$136 cm^{-1} are shown in (b1), (b2), and (b3). Nine IR-active modes observed throughout the T range of this study are marked with black bars in (c). At least three new modes (red arrows) are seen at 170 K. The displacement patterns for IR Fano mode at $\sim$208 cm^{-1} are shown in (c1). Two-dimensional (2D) atomic displacement patters of A_g modes involving both chiral and breathing displacements: (d) K(2) based $\sim$112 cm^{-1} and (e) Fe(2) 267 cm^{-1}. All displacements are not to scale. Two peaks at $\sim$29 and 95 cm^{-1} marked by * in (b) are due to plasma lines of Kr laser.

measured vibration frequencies summarized in Table I. The computed B_g mode at 66.4 cm^{-1} is not observed. The B_g vibration at $\sim$117.3 cm^{-1} submerges to the broad B_g mode at $\sim$100 cm^{-1}, Fig. 1(a), and is revealed in the fit. Importantly, two A_g modes at 79.9 and 89.0 cm^{-1} cannot be reproduced in nonmagnetic (NM) $I4/m$ $\sqrt{5} \times \sqrt{5}$ structure, either undoped $K_{0.8}Fe_{1.6}Se_2$ or vacancy-free KFe_2Se_2, also computed in this work but not listed in Table I. Therefore, accounting for the spin degree of freedom is essential for accurate mapping of

the observed Raman modes. The eight out of nine observed IR-active modes at 300 K are assigned; Table I and Fig. 1(c). The remaining E_u mode at $\sim$278 cm^{-1} is likely due to finite Fe(1) population in the superconducting sample: an extra E_u mode appears in NM vacancy-free $I4/m$ at 294 cm^{-1}. In summary, the observed Raman and IR vibration frequencies above $\sim$200–250 K are in good agreement with computed frequencies. Below 200–250 K, new Raman modes at $\sim$165, 201, and 211 cm^{-1} and IR-active modes at $\sim$99, 171, and

TABLE I. Assignment of observed Raman and IR vibration modes in $K_{0.75}Fe_{1.75}Se_2$ based on comparison with first-principles calculations utilizing pseudopotentials. Raman and IR modes which appear below $T_1 \sim 250$ K are marked by $+$ and $\#$. The Lorentz parameters for Raman and ab-plane IR modes, respectively, at 3 and 35 K were obtained from fit to the experimental data shown in Fig. 1. Here ω_i and Γ_i (in cm^{-1}) are the frequency and full width at half maximum (FWHM), of the ith mode. Error bars estimated from covariance are 0.2–0.4 and 0.4–2.0 cm^{-1} for ω_i and Γ_i. Raman data from Ref. 15 and IR data from Ref. 19 are shown for comparison. Computed vibration frequencies are shown for $I4/m$ structure. Total number of modes is less than in Eq. (1) because K(1) and acoustic modes are not computed/omitted. Vibration frequencies in $I4$ less than 10 cm^{-1} apart are not shown in this Table. A_g, B_g, and E_u modes in $I4/m$ becomes, respectively, A, B, and E modes in $I4$; refer to Sec. IV.

AFM, $I4/m$	Raman (ω, Γ)	Ref. 15	IR (ω, Γ)	Ref. 19
$63.6A_g$	67.6, 3.5	66.3		
$79.9A_g$	81.0, 6.1			
$89.0A_g$	111.8, 15.0			
$108.2A_g$	124.8, 11.1	123.8		
$126.0A_g$	Fano 135.9	134.6		
$173.5A_g$	182.5, 3.4			
$211.1A_g$	205.3, 3.6	202.9		
$236.0A_g$	Fano 242.3	239.4		
$265.9A_g$	267.0, 5.3	264.6		
$57.9B_g$	63.1, 6.2	61.4		
$66.4B_g$				
$98.2B_g$	100.6, 12.8	100.6		
$117.3B_g$	103.3, 2.1			
$134.9B_g$	Fano 143.6	141.7		
$206.0B_g$	195.3, 2.6			
$224.0 B_g$	216.1, 3.0	214.3		
$262.7B_g$	Fano 277.1	274.9		
$59.0E_g$				
$79.9E_g$				
$95.1E_g^{\#}$			98.9, 8.2	102.3
$104.5E_g$				
$156.9E_g^{\#}$			171.2, 4.9	
$206.5E_g$				
$224.0E_g$				
$251.3E_g^{\#}$			246.3, 5.	
$61.1A_u$				
$92.7A_u$				
$96.3A_u$				
$172.4A_u^{+}$	165.2, 3.6			
$212.4A_u^{+}$	211.0, 1.4			
$249.7A_u$				
$271.0A_u$				
$67.7B_u$				
$76.0B_u$				
$89.3B_u$				
$116.2B_u$				
$181.9B_u^{+}$	200.5, 3.4			
$240.5B_u$				
$273.0B_u$				
$62.5E_u$			63.8, 7.1	65.2
$73.9E_u$			74.2, 6.1	73.6
$85.9E_u$			91.3, 16.	93.7
$96.5E_u$			118.5,10.	121.9

TABLE I. *(Continued.)*

AFM, $I4/m$	Raman (ω, Γ)	Ref. 15	IR (ω, Γ)	Ref. 19
$140.7E_u$			150.1, 4.0	151.7
$219.3E_u$			Fano 207.6	208.3
$233.3E_u$			236.6, 4.4	238.3
$268.3E_u$			267.2, 6.1	267.1
			276.1, 4.9	278.6

246 cm^{-1} show up. Their vibration frequencies correspond well to the computed frequencies of Raman-active A, B, and IR-active E in the $I4$ structure; Table I.

Displacement patterns of selected vibration modes are illustrated in Fig. 1. Raman modes shown in (a1) and (b1) correspond to Fe B_{1g} and As A_{1g} vibrations in the 122 iron-arsenides.[25] In AFM $I4/m$ both modes got finite (x,y) displacements. The $B_g \sim 100$ cm^{-1} mode is dominated by in-plane K displacements with some admixture of Se and Fe displacements. Its large T-independent linewidth is related to static disorder associated with K(2) sites. The $A_u \sim 172.4$ cm^{-1} patterns are shown in (b2). Being non-Raman active in the AFM $I4/m$ phase it becomes new Raman mode A in the low-T phase AFM $I4$; Fig. 1(b2). Figure 1 visualizes atomic displacement of one IR-active (c1) and two out of four observed Raman-active Fano modes (a3 and b3) discussed in this paper. The striking feature of all but Se-based $A_g \sim 136$ cm^{-1} is essential involvement of Fe(2) atomic displacements. In $K_{0.8}Fe_{1.6}Se_2$ Fe atoms carry magnetic moment as large as 3.3 μ_B,[4] while electronic structure near E_f is dominated by Fe d states.[3] The Fano modes coupling to electronic and magnetic degrees of freedom are explored in the following section.

B. Origin of Fano vibration modes

Asymmetric line shapes are characteristic of Fano resonances arising from coupling between the phonons and an electronic continuum, electronic or magnetic in origin. Dipole transition in the IR absorption does not directly couple the AFM excitations, but couples charge carriers. Raman
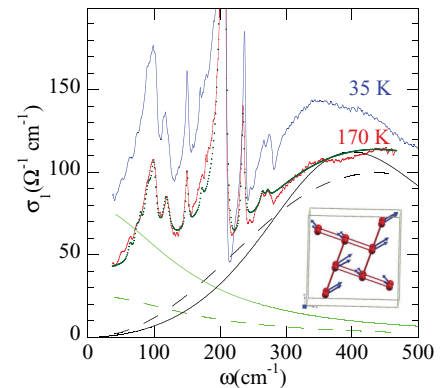

FIG. 2. (Color online) Optical conductivity at 35 K (blue) and 170 K (red) along with a fitting curve (dark green dots). Drude components (green) and MIR Lorentz terms (black) are shown with solid(dashed) curves for 35(170) K. Insert: c-axis view of ab- plane displacement patterns (not up to scale) of the Fe(2) atoms.
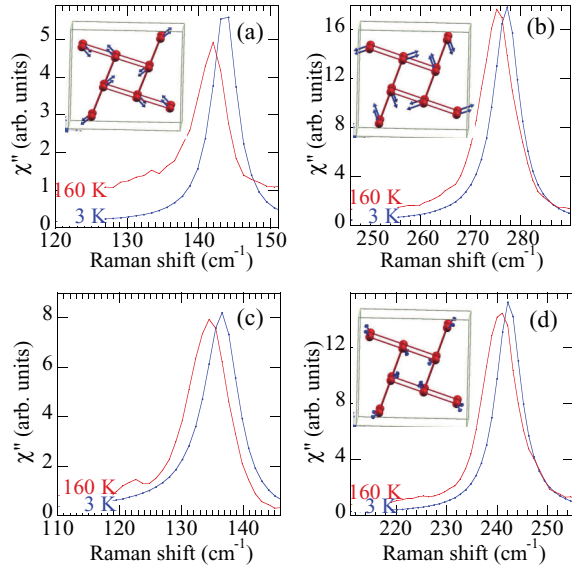
FIG. 3. (Color online) Raman Fano modes for (a) $\sim$142 and (b) $\sim$277 cm^{-1} in RL and (c) $\sim$137 and (d) $\sim$242 cm^{-1} in RR. Insets: c-axis view of ab-plane displacement patterns (not up to scale) of the Fe(2) atoms. The 3D displacement patterns are shown in Fig. 1.

scattering probes both electronic and magnetic excitations. The 208-cm^{-1} IR and $\sim$144-, 242-, and 277-cm^{-1} Raman Fano modes are dominated by Fe(2) atomic displacements. Interestingly, the IR mode gets more asymmetric (Fig. 2) while four Raman modes [Figs. 3(a)–3(d)] become more symmetric on cooling.

The optical conductivity at 35 and 170 K is shown in Fig. 2. Taking 170-K spectrum as an example, the experimental conductivity is fitted as a sum of the Drude peak (dashed green), the broad Lorentz component (dashed black) describing interband transition at $\sim$400 cm^{-1}, the beginning of midinfrared (MIR) peak, and 11 Lorentz and 1 Fano phonon modes. Both Drude and MIR become slightly more coherent and better pronounced as temperature decreases to 35 K. At frequency of Fano mode, the Dude contribution increases, while the MIR contribution slightly decreases. Therefore, enhancement in the IR Fano peak asymmetry is due to the vibration coupling to charge carriers in the Drude tail.

Four Fano Raman modes are presented in Figs. 3(a)–3(d) at 3 and 160 K. They were obtained by removal of fitted in phonons from data shown in Figs. 1(a) and 1(b). Clearly, all Raman modes exhibit similar T dependence: (a) they are less symmetric, and (b) they characterized by larger background at 160 K than at 3 K. The observed behavior is reminiscent of T dependence of a new mode observed in AFM 122 systems. The mode appears at T_N as a Fano-shaped one and it becomes progressively more symmetric with temperature decrease. The Fano peak derives from vibration coupling to magnetic continuum, the AFM spin fluctuations.

C. Temperature dependence of Raman mode linewidth and phonon frequencies

Selected linewidth and phonon frequencies as function of temperature are shown in Fig. 4. The T-dependent phonon
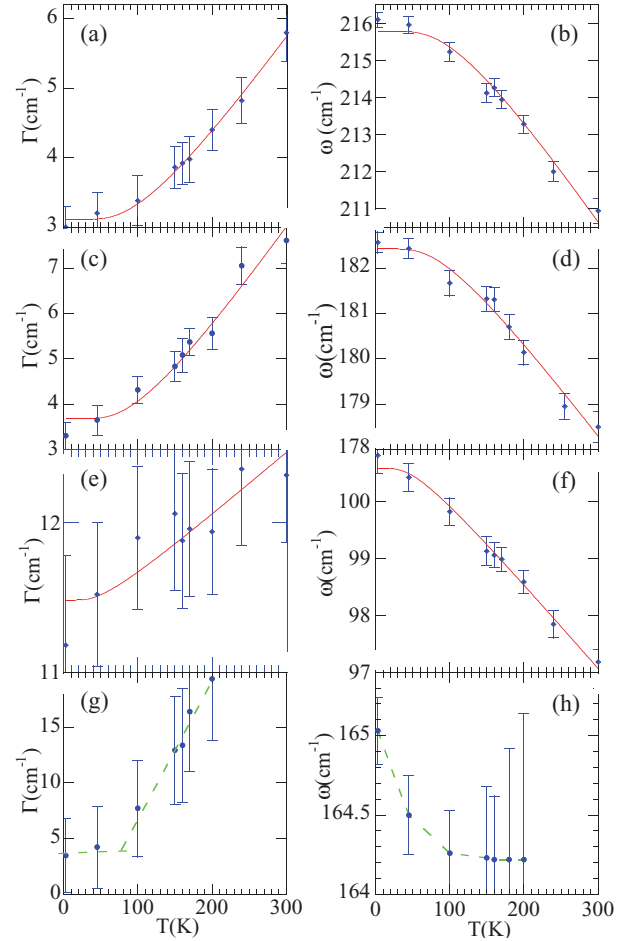

FIG. 4. (Color online) Linewidth (first row) and subsequent phonon frequencies (second row) of Fe(2) $B_g \sim$ 216-, Se(2) $A_g \sim$ 182-, K(2) $B_g \sim$ 100-, and Se(1) $A_g \sim$ 165-cm^{-1} modes. Solid red lines describe two-phonon anharmonic decay (Ref. 26). Dashed green lines are guided to the eye. The atomic displacement patterns of the modes are visualized in Fig. 1 (a1, b1, a2, and b2).

frequencies qualitatively agree with those reported by Zhang *et al.* in K$_{0.8}$Fe$_{1.6}$Se$_2$ (Fig. 5 in Ref. 15) and by Lazarević *et al.* in isostructural K$_{0.88}$Fe$_{1.63}$S$_2$ [Figs. 3(b)–3(j) in Ref. 16]. In the latter work, the authors concluded that the Raman-active phonon energies in the range 80–300 K are fully driven by anharmonicity effects.[16] The interpretation offered in the present work is different: the residual linewidth is compatible [Figs. 4(a)–4(c)] or larger [Fig. 4(e)] than the temperature-dependent increment between 3 and 300 K. Therefore, self-energy of non-Fano phonons (i.e., at $\sim$195 and 216 cm^{-1} in B_g and at $\sim$68, 205, and 267 cm^{-1} in A_g channels) consist of approximately equal contributions of two-phonon lattice anharmonicity on one hand and bare self-energy and broadening due to intrinsic defects on the other. Self-energy of the $\sim$100 cm^{-1} mode involving the K(2) atomic displacements is dominated by inhomogeneous broadening. The new $\sim$165 cm^{-1} mode appearing at T_1 in the range 200–250 K becomes fully coherent below $\sim$40–60 K: the linewidth presented in Fig. 4(g) quickly reduces by $\sim$5 times as temperature decreases from 200 to 60 K, followed
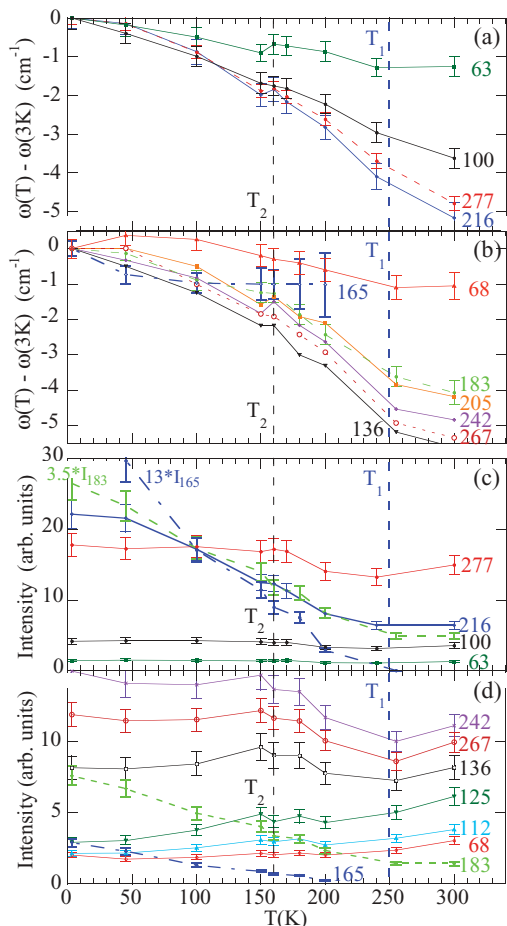
FIG. 5. (Color online) Temperature dependence of selected phonon frequencies (a),(b) and intensities (c),(d). Some error bars are omitted in (b) for clarity. T_1 and T_2 mark temperatures of structural phase transition at $\sim$250 K and phonon anomalies at $\sim$160 K. In (c) intensity of the Fe(2)-based $B(B_g) \sim 216$ cm^{-1} (solid blue line) scales almost perfectly to 3.5 ± 0.2 times intensity of Se(2)-based $A(A_g) \sim 183$ cm^{-1} (dashed green line) in the range 45–250 K. It also satisfactorily scales to 13 ± 1 times intensity of the Se(1)-based $A \sim 165$ cm^{-1} (dot-dashed blue line) in the range $\sim$100–200 K. Note that there are four Se(2) per one Se(1) atom.

by saturation below $\sim$40 K. The mode hardens on cooling by $\sim$1.0 cm^{-1} [Fig. 4(h)] in the traceable T range.

IV. DISCUSSION

The new 165-cm^{-1} mode appearing at T_1 in the range 200–250 K [inset of Fig. 1(b)] usually referred to as seen at T_1 below $\sim$250 K throughout this paper, is not Raman active in the $I4/m$ phase (Table I), fully symmetric in character, and it quickly becomes coherent with T decrease [Fig. 3(g)]. The question arises whether this mode signifies crystal symmetry lowering on a structural phase transition. If it is associated with symmetry lowering, it would become the allowed phonon mode in one of the subgroups of C_{4h}. The C_{4h} encompass the C_4 (loss of inversion and rotationreflection), C_{2h} (loss of fourth-order rotation axis), S_4 (loss of inversion and fourth-

order rotation axis), C_2 (loss of inversion, fourth-order rotation axis, and rotation reflection), and C_1 (primitive) subgroups. We did not observe leaking of four-fold axis symmetry that would results in the cross-polarization intensity leakages beyond small leakages of polarization optics which do not correlate with the temperature dependence of the 165-cm^{-1} mode. Thus, C_{2h}, C_2, and C_1 subgroups are excluded. The S_4 (space group 82) is excluded because there is no new A-type Se(1) mode associated with the transition. Therefore, $I4/m$ (C_{4h}, space group 87) becomes $I4$ (C_4, space group 79). From the factor-group analysis A_g, B_g, and E_u modes in C_{4h} becomes, respectively, A, B, and E modes in C_4. Instead of $9A_g + 8B_g$ Raman-active and $8E_u$ infrared-active modes in the high-T $I4m$ phase one would expect to encounter $17A + 15B$ Raman and $17E$ IR-active modes in the low-T phase under the measured geometry. Here we excluded acoustic and Fe(1)-related modes, since the Fe(1) site is a mostly empty site in $K_{0.75}Fe_{1.75}Se_2$. The Raman-active modes do not overlap with ab-plane IR-active modes, not only in high- but in low-T phases. This explains the seemingly puzzling absence of IR mode leakages into the Raman spectra noted in Sec. III. Since new Raman modes (at $\sim$165-, 201-, and 211-cm^{-1} and IR-active modes (at $\sim$99, 171, and 246 cm^{-1}) appears below T_1 and those modes are non-Raman (non-IR) active A_u (E_g) or silent B_u in $I4m$ (Table I) we suggest that $K_{0.75}Fe_{1.75}Se_2$ undergoes $I4/m \rightarrow I4$ structural phase transition accompanied by loss of inversion symmetry at T_1 below $\sim$250 K. Our first-principles calculations utilizing pseudopotentials also narrowly favor $I4$ over the $I4/m$ structure. The small total-energy difference is likely because computations do not include all correlations and/or the calculations are performed for the undoped $K_{0.8}Fe_{1.6}Se_2$.

Temperature dependence of selected phonon frequencies and intensities are shown in Figs. 5(a) and 5(b) and 5(c) and 5(d), respectively. Apart from the structural phase transition at T_1 below $\sim$250 K, clearly there is a second characteristic temperature, $T_2 \sim$160 K. At T_2 the majority of phonon vibration frequencies exhibit consistent discontinuity up to $\sim$0.3 cm^{-1} [Figs. 5(a) and 5(b)], while quite a few modes display $dI(T)/dT$ slop changes in their intensity vs temperature dependencies [Figs. 5(c) and 5(d)]. Since no new vibration modes (Raman or IR) are observed below the T_2, the T_2 does not constitute a structural phase transition, but is rather referred to as a phonon anomaly temperature. An anomaly of a single A_g mode at 66 cm^{-1} at 160 K was mentioned by Zhang *et al.*[15] We would like to point out that the phonon anomalies seen at $T_2 \sim$160 K involve a majority of measured Raman modes.

From experimental data at hand we could point out two implications of the observed structural phase transition on low-T properties of $K_{0.75}Fe_{1.75}Se_2$. First, symmetry of the Se(1,2)-Fe(2) slab is broken at T_1, the sample becomes ferroelectric, and c-axis structural distortions within the slab appear to build up on cooling. This is seen in Raman phonon peak intensities, Figs. 5(c) and 5(d), which are directly proportional to the polarizability tensor. As the sample enters the low-T phase ($T < T_1$), the polarizability of quite a few Raman-active modes build up until $\sim T_2$, followed by saturation at $T < T_2$ (B symmetry at 63, 100.6, and 277; A symmetry at 81 and 267, Fano shape 136 and 242 cm^{-1}) or reduction (A symmetry at

68, 112, and 125 cm^{-1}). However, the polarizabilities of the Fe(2)-based B mode at $\sim$216, As(2)-based A mode at $\sim$183, and As(1)-based A mode at $\sim$165 cm^{-1} continue to build up until $\sim$45, 3, and 3 K, respectively. The scaling relationships among the three are shown in Fig. 5(c). The scaling is not surprising, giving the similar displacement patterns of the modes along the c axis [Fig. 1(a1), (b1), and (b2)], so that their Raman activities are driven by the polarizability of the electronic orbitals forming the Fe-Se slabs. In iron-arsenides (122 systems) the Fe-As slab is perfectly symmetric and the Raman-active As-based A_{1g} mode has extremely low intensity (polarizability) if measured in the same geometry.[25] It becomes visible upon doping destroying the symmetry of the slab. In K$_{0.75}$Fe$_{1.75}$Se$_2$, intrinsic population of Fe and K vacancies makes the Se(2)-based $A_g \sim 183$ cm^{-1} mode effortlessly visible at room temperature. The atomic displacements associated with the $I4/m \rightarrow I4$ phase transition which have sizable ab-plane components are likely quenched below T_2, while c-axis displacements continue to build up on cooling. The second implication concerns the temperature dependence of low-frequency optical conductivity shown in Fig. 1(c). The conductivity displays weak temperature dependence above T_1 followed by a faster increase below T_2, in agreement with similar temperature dependence reported by Homes *et al.*[19]

The onset of superconductivity at $\sim$30 K has little effect on phonons. Using 3 and 45 K data points, the upper estimated phonon energy shifts are -0.3 ± 0.4 cm^{-1} ($|\Delta\omega|/\omega \sim 0.44\%$) for 67.6 cm^{-1} and $+0.6 \pm 0.4$ cm^{-1} ($|\Delta\omega|/\omega \sim 0.36\%$) for 165.0-cm^{-1} modes. Small frequency renormalization implies either a weak e-ph interaction or that the phonons used in our analysis belong to the AFM phase in the phase separated models:[6,7,10–14] spectator AFM phonons would not feel the onset of the superconductivity, unless via the proximity effect.

V. CONCLUSIONS

Raman scattering and optical conductivity were used to determine lattice vibration frequencies of superconducting crystal K$_{0.75}$Fe$_{1.75}$Se$_2$ in the temperature range 3–300 K. 19 Raman-active and 12 IR-active modes are observed at 3 K. The $\sim$136-, 143-, 242-, and 277-cm^{-1} Raman and $\sim$208-cm^{-1} IR mode exhibit Fano-like shape. The Raman Fano modes are due to the vibration coupling to AFM spin fluctuations, while the IR mode is coupled to charge carriers in the low-frequency part of optical conductivity. Raman phonon linewidths contain approximately equal contributions of two-phonon lattice anharmonicity on one hand and bare self-energy and broadening due to intrinsic defects on the other hand. The K$_{0.75}$Fe$_{1.75}$Se$_2$ undergoes $I4/m$ (space group 87) $\rightarrow I4$ (space group 79) structural phase transition at T_1 below $\sim$250 K. Several modes which are not Raman and IR active in the measured geometry in $I4/m$ become visible in the $I4$ phase including Raman modes at $\sim$165, 201, and 211 cm^{-1} and IR-active modes at $\sim$99, 171, and 246 cm^{-1}. Weak phonon anomalies are also observed at $T_2 \sim 160$ K. Symmetry of the Se(1,2)-Fe(2) slab is broken at T_1. ab-plane structural distortions are likely quenched below T_2, while c-axis structural distortions within the slab continue to build up on cooling down to 3 K.

ACKNOWLEDGMENTS

[1] J. Guo, S. Jin, G. Wang, S. Wang, K. Zhu, T. Zhou, M. He, and X. Chen, Phys. Rev. B **82**, 180520(R) (2010); A. F. Wang, J. J. Ying, Y. J. Yan, R. H. Liu, X. G. Luo, Z. Y. Li, X. F. Wang, M. Zhang, G. J. Ye, P. Cheng, Z. J. Xiang, and X. H. Chen, *ibid.* **83**, 060512(R) (2011).

[2] R. H. Liu, X. G. Luo, M. Zhang, A. F. Wang, J. J. Ying, X. F. Wang, Y. J. Yan, Z. J. Xiang, P. Cheng, G. J. Ye, Z. Y. Li, and X. H. Chen, Europhys. Lett. **94**, 27008 (2011).

[3] X.-W. Yan, M. Gao, Z.-Y. Lu, and T. Xiang, Phys. Rev. B **83**, 233205 (2011).

[4] W. Bao, Q.-Z. Huang, G.-F. Chen, M. A. Green, D.-M. Wang, J.-B. He, and Y.-M. Qiu, Chin. Phys. Lett. **28**, 086104 (2011).

[5] Y. J. Yan, M. Zhang, A. F. Wang, J. J. Ying, Z. Y. Li, W. Qin, X. G. Luo, J. Q. Li, J. Hu, and X. H. Chen, Sci. Rep. **2**, 212 (2012).

[6] Z. Wang, Y. J. Song, H. L. Shi, Z. W. Wang, Z. Chen, H. F. Tian, G. F. Chen, J. G. Guo, H. X. Yang, and J. Q. Li, Phys. Rev. B **83**, 140505 (2011).

[7] A. Ricci, N. Poccia, G. Campi, B. Joseph, G. Arrighetti, L. Barba, M. Reynolds, M. Burghammer, H. Takeya, Y. Mizuguchi, Y. Takano, M. Colapietro, N. L. Saini, and A. Bianconi, Phys. Rev. B **84**, 060511 (2011).

[8] J. Zhao, H. Cao, E. Bourret-Courchesne, D.-H. Lee, and R. J. Birgeneau, arXiv:1205.5992v1 [cond-mat.supr-con].

[9] D. A. Torchetti, M. Fu, D. C. Christensen, K. J. Nelson, T. Imai, H. C. Lei, and C. Petrovic, Phys. Rev. B **83**, 104508 (2011).

[10] R. H. Yuan, T. Dong, Y. J. Song, P. Zheng, G. F. Chen, J. P. Hu, J. Q. Li, and N. L. Wang, Sci. Rep. **2**, 221 (2012).

[11] A. Charnukha, A. Cvitkovic, T. Prokscha, D. Pröpper, N. Ocelic, A. Suter, Z. Salman, E. Morenzoni, J. Deisenhofer, V. Tsurkan, A. Loidl, B. Keimer, and A. V. Boris, Phys. Rev. Lett. **109**, 017003 (2012).

[12] Y. Texier, J. Deisenhofer, V. Tsurkan, A. Loidl, D. S. Inosov, G. Friemel, and J. Bobroff, Phys. Rev. Lett. **108**, 237002 (2012).

[13] G. Friemel, J. T. Park, T. A. Maier, V. Tsurkan, Yuan Li, J. Deisenhofer, H.-A. Krug von Nidda, A. Loidl, A. Ivanov, B. Keimer, and D. S. Inosov, Phys. Rev. B **85**, 140511(R) (2012).

[14] W. Li, H. Ding, P. Deng, K. Chang, C. Song, K. He, L. Wang, X. Ma, J.-P. Hu, X. Chen, and Q.-K. Xue, Nat. Phys. **8**, 126 (2012).

[15] A. M. Zhang, K. Liu, J. H. Xiao, J. B. He, D. M. Wang, G. F. Chen, B. Normand, and Q. M. Zhang, Phys. Rev. B **85**, 024518 (2012).

[16] N. Lazarević, H. Lei, C. Petrovic, and Z. V. Popović, Phys. Rev. B **84**, 214305 (2011).

[17] A. M. Zhang, K. Liu, J. H. Xiao, J. B. He, D. M. Wang, G. F. Chen, B. Normand, and Q. M. Zhang, arXiv:1105.1198v2 [cond-mat.supr-con].

[18] Z. G. Chen, R. H. Yuan, T. Dong, G. Xu, Y. G. Shi, P. Zheng, J. L. Luo, J. G. Guo, X. L. Chen, and N. L. Wang, Phys. Rev. B **83**, 220507(R) (2011).

[19] C. C. Homes, Z. J. Xu, J. S. Wen, and G. D. Gu, Phys. Rev. B **85**, 180510(R) (2012).

[20] S. Baroni, A. Dal Corso, S. de Gironcoli, and P. Giannozzi, 2001, http://www.pwscf.org.

[21] D. Vanderbilt, Phys. Rev. B **41**, 7892 (1990).

[22] D. R. Hamann, M. Schlüter, and C. Chiang, Phys. Rev. Lett. **43**, 1494 (1979).

[23] H. J. Monkhorst and J. D. Pack, Phys. Rev. B **13**, 5188 (1976); J. D. Pack and H. J. Monkhorst, *ibid.* **16**, 1748 (1977).

[24] S. Baroni, S. de Gironcoli, A. Dal Corso, and P. Giannozzi, Rev. Mod. Phys. **73**, 515 (2001).

[25] A. P. Litvinchuk, V. G. Hadjiev, M. N. Iliev, Bing Lv, A. M. Guloy, and C. W. Chu, Phys. Rev. B **78**, 060503(R) (2008).

[26] M. Balkanski, R. F. Wallis, and E. Haro, Phys. Rev. B **28**, 1928 (1983).